Phase-Sensitive Intracellular Doppler Fluctuation Spectroscopy

Honggu Choi,[1] Zhe Li,[1] Kwan Jeong,[1,2] Jessica Zuponcic,[3] Eduardo Ximenes,[3] John Turek,[4] Michael Ladisch,[3,5] and David D. Nolte[1,*]

[1] *Department of Physics and Astronomy, Purdue University, 525 Northwestern Ave, West Lafayette, Indiana 47907, USA*

[2] *Department of Physics and Chemistry, Korea Military Academy, 574 Hwarang-ro, Nowon-gu, Seoul 01805, Republic of Korea*

[3] *Department of Agricultural and Biological Engineering and the Laboratory of Renewable Resources Engineering, Purdue University, West Lafayette, Indiana 47907, USA*

[4] *Department of Basic Medical Science, Purdue University, 625 Harrison St, West Lafayette, Indiana 47907, USA*

[5] *Weldon School of Biomedical Engineering, Purdue University, West Lafayette, Indiana 47907, USA*

(Received 11 August 2020; revised 4 January 2021; accepted 6 January 2021; published 18 February 2021)

Dynamic light scattering from three-dimensional intracellular motions in living tissues or biopsies creates dynamic speckle due to broadband Doppler shifts that are recorded as broadband spectra obtained from speckle fluctuation spectroscopy. Doppler frequency shifts from active intracellular motion extend across three orders of magnitude from 10 mHz to 10 Hz. Biodynamic imaging is a full-field optical coherence tomography technique performed with low-coherence digital holography. The holographic reconstruction allows phase recovery, but mechanical stability limitations favor homodyne detection over heterodyne detection because homodyne is relatively insensitive to phase drift. However, by obtaining phase-displacement distributions from consecutive frames, the phase excursions form a robust probability distribution. The phase-probability density function of the phase-displacement distribution captures average phase displacements over time and is used to reconstruct stable heterodyne spectra. Phase-sensitive biodynamic imaging is applied to detect Levy-stable distributions from living tissue that may reflect heavy-tailed anomalous transport within intracellular media.

DOI: 10.1103/PhysRevApplied.15.024043

I. INTRODUCTION AND BACKGROUND

The mechanical properties of biological systems can be investigated by optical techniques. For example, optical coherence tomography [1] and fluorescence imaging [2] can visualize microscale dynamics in real time to provide a better understanding of biological dynamics. Dynamic light scattering (DLS) applications in chemistry and biology have a long history [3], but coherence-gated dynamic light scattering was established in living tissue using nonlinear optical coherence imaging [4] followed by initial studies in optical coherence tomography (OCT) [5]. The effects of metabolism and drugs on DLS in living tumor tissues are measured using digital holography and biodynamic imaging [6–10] followed by expanding DLS studies using OCT [11–15], including field-based techniques [16]. Subsequent low-coherence studies to extract intracellular dynamics investigate the effects of anticancer treatments on xenograft tumors [17], measured metabolic activity [18], and cytoskeletal drugs [6,19], as well as preclinical [20] and human clinical trials [21] of cancer therapies. Biodynamic imaging (BDI) provides a quantitative analysis of intracellular dynamics using fluctuation spectroscopy to measure the broadband Doppler shifts caused by DLS from three-dimensional intracellular dynamics of biological specimens. Doppler shifts cause dynamic interference in speckle intensity, and the power spectral density of the Doppler signal is acquired by performing temporal Fourier transforms of the dynamic speckle intensity fluctuations.

The Doppler signal is intrinsically carried by the phase of speckle images reconstructed from digital holograms. However, difficulties in analyzing the phase information arise due to inherent phase instability caused by external mechanical perturbations.

Heterodyne detection is highly sensitive to phase deviations, and phase noise makes the interpretation of the heterodyne power spectral density challenging. Many methods are proposed to stabilize the phase information of functional images by controlling the optical design [22–24] and improving mechanical isolation. However, such physical stabilization approaches can be expensive, complicated, and incomplete. Here, we describe an alternative approach that captures a stabilized and sensitive

*nolte@purdue.edu

Doppler power spectrum through digital postprocessing in a method that acquires a phase-probability density function (Φ_{PDF}) of Doppler phase displacements. This provides an intuitive dynamic picture of the target, and the Doppler power spectral density derived from Φ_{PDF} shows greater sensitivity and stability than those of conventional heterodyne power spectra. As an example, we show that changes in Φ_{PDF} shape acquired by phase-sensitive biodynamic imaging induced by bacterial infections of epithelial cells demonstrate invasive bacterial dynamics characterized by random-walk models with anomalous ballistic motions [25].

II. BIODYNAMIC LIGHT SCATTERING

A. Biodynamic imaging

Figure 1(a) shows a schematic of the BDI system used in this work. BDI uses a Mach-Zehnder interferometer configuration with a low-coherence light source ($\lambda = 840$ nm, Superlum S-840-B-I-20). Backscattered light from the sample is collected by the $4f$ system ($f = 15$ cm) and delivered at the IP. The Fourier lens ($f = 5$ cm) performs a Fourier transform and a Fourier image is formed at the Fourier plane (FP). The Fourier image interferes with the off-axis reference signal from the reference arm and forms a holographic image at the FP. The low-coherence interferometry provides coherence gating [26] that selects light scattered preferentially from a path-length-selected optical section. At a given position of the optical path delay at the reference arm, the optical path length of the reference arm matches the optical path length of light scattered from a specific depth inside the target to within the coherence length (~20 μm). The coherence gating enables the direct reconstruction of *en face* sections that can be scanned in depth to extract three-dimensional images of millimeter-sized samples. To reject the background, all fluctuation analyses are performed with the reconstructed images. The principle difference between low-coherence Fourier-domain digital holography [27] and low-coherence image-domain full-field OCT [28] is the sensitivity to dynamics.

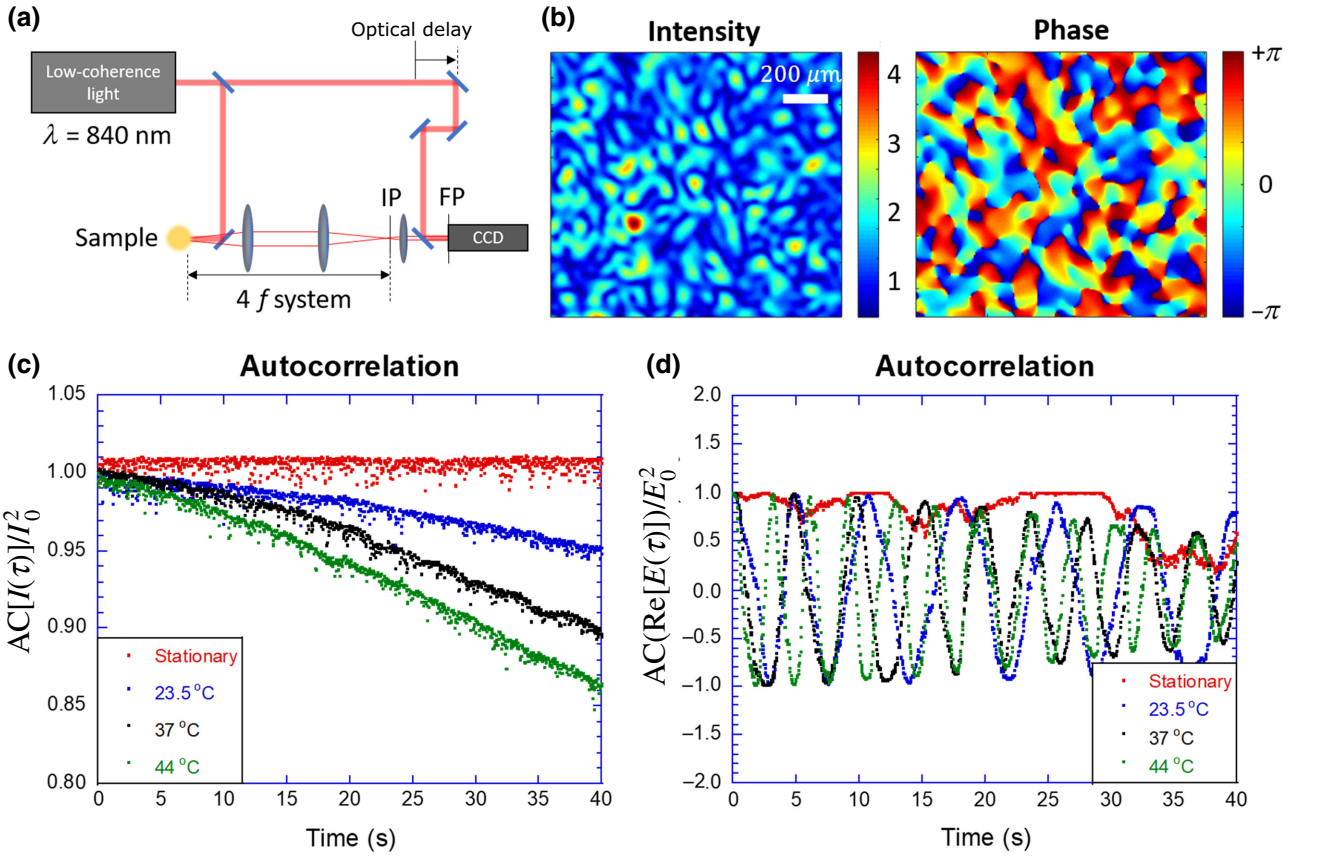

FIG. 1. Doppler shifts are induced by scattering from slowly moving targets. (a) Schematic diagram of the BDI system and (b) hologram intensity and phase at the Fourier plane (FP) from a small sheet of paper floating on water. Speckle at the FP is obtained by spatial carrier frequency demodulation of the hologram. Phase profile contains multiple optical vortices. (c) Autocorrelation (AC) of the dynamic speckle intensity and (d) field modulation at the image plane (IP). Stationary case measures the dynamic speckle of a sheet of paper at the bottom of a well. Temperatures are varied between 23.5 and 44 °C to change the evaporation rate of water, and hence, the speed of the target.

Biodynamic imaging is performed with the coherence gate set at depths greater than 200 μm in dense epithelial tissue using broad-area illumination without spatial filtering, which maximizes dynamic speckle sensitivity, but with a trade-off in spatial resolution.

Holographic images are recorded by using a CCD camera (Basler acA-1920) with a 25 Hz sampling frequency. Recorded holograms are digitally reconstructed by performing a spatial Fourier transform to generate optical coherence images (OCIs) by filtering out the background and edge truncation rods. The time series of reconstructed off-axis holograms display temporally fluctuating dynamic speckle. Digitally reconstructed dynamic speckle from a holographic image at the FP carries both intensity and phase information. A homodyne power spectrum of the broadband Doppler signal is obtained by performing a temporal Fourier transform on the intensity time series from each pixel [8]. The Doppler power spectrum within the frequency band between 0.01 and 12.5 Hz corresponds to velocities between 3 nm/s to 3 μm/s [10]. To analyze the phase information of the dynamic speckle, homodyne and heterodyne Doppler power spectra are acquired and compared.

B. Heterodyne and homodyne detection

The power spectrum obtained from the temporal intensity information defines the homodyne power spectrum as

$$S_{\mathrm{hom}}(\omega) = \frac{1}{N}\sum_{x,y}^{N}\left|\int I_{x,y}(t)e^{i\omega t}dt\right|^2, \qquad (1)$$

where $I_{x,y}(t)$ is the intensity time series at a spatial coordinate (x,y) and is averaged over N pixels. The power spectrum from Eq. (1) does not include the phase information because it is conjugated. Biodynamic homodyne spectra are relatively stable against mechanical perturbations of the optical system and provide a reliable means to monitor changes in intracellular Doppler light scattering. However, coherence-domain detection using digital holography [29] intrinsically captures phase information, which would be valuable to retain if it could be stabilized against mechanical perturbations. The importance of the phase is particularly useful in the case of Doppler light scattering because of the role of phase in any form of directed motion, such as ballistic transport that is common in intracellular transport.

A heterodyne power spectrum incorporates the phase information directly from the field reconstruction [30] by performing temporal Fourier transforms on complex-value fields by

$$S_{het}(\omega) = \frac{1}{N}\sum_{x,y}^{N}\left|\int E(t)e^{i\phi(t)}e^{i\omega t}dt\right|^2, \qquad (2)$$

where $E_{x,y}(t)$ is the real-value amplitude and $e^{i\phi(t)}$ contains the phase from the time series of the complex-value electric field of the OCI frames [Fig. 1(a)]. The complex field of the OCI is acquired directly from the off-axis digital holographic reconstruction. The average heterodyne power spectrum is acquired by performing a temporal Fourier transform on each pixel of the reconstructed OCI time series and averaging over the dynamic speckle.

III. HETERODYNE DOPPLER FREQUENCY CALIBRATION

A. Heterodyne detection of sub-Hz Doppler shift

The surface evaporation rate of water varies with temperature [31], and the estimated speed of the water surface caused by evaporation is around 100 nm/s, which is an appropriate speed to calibrate phase-sensitive detection. To measure Doppler shifts caused by surface evaporation, a circular-shaped paper sheet with a 3 mm radius and 15 μm thickness is prepared. The paper floats on the water surface of a multiwell plate and during evaporation the paper moves vertically towards the bottom of the well. Low-coherence light illuminates the paper from below, and an interference pattern is formed at the Fourier plane of the digital holography system. The evaporation rate is constant, the vertical motion induced by the evaporation is steady, and the dynamic speckle fluctuations with different temperatures are demonstrated in Figs. 1(c) and 1(d). The evaporation speed is measured at three different water temperatures of 23.5, 37, and 44 °C.

When the floating paper at the water surface is at the coherence-gated depth, the holographic dynamic speckle is recorded with 25 frames/s for 80 s (bandwidth 0.02 to 12.5 Hz). The holographic reconstruction of dynamic speckle is conducted by performing a spatial Fourier transform of holograms at the Fourier plane. An example of reconstructed speckle is shown in Fig. 1(b). The time series of amplitude and field information are compared in Figs. 1(c) and 1(d). The characteristics of dynamic speckle show visible modulation caused by the Doppler shifts with constant velocities.

B. Heterodyne and homodyne power spectra

To investigate the power spectra of the dynamic speckle shown in Fig. 1, a Fourier transform of the 2048-frame time series has 1024 positive and negative nonzero frequency components and a dc component at $\omega = 0$. Positive and negative nonzero Fourier components are symmetric for a homodyne power spectrum [Fig. 2(a)], while the negative components of the heterodyne spectrum are plotted in Fig. 2(b). The heterodyne power spectrum has an asymmetric shape biased by the directed motion of the evaporating water surface. The heterodyne power spectrum of the one-sided Fourier spectrum containing the Doppler peak is

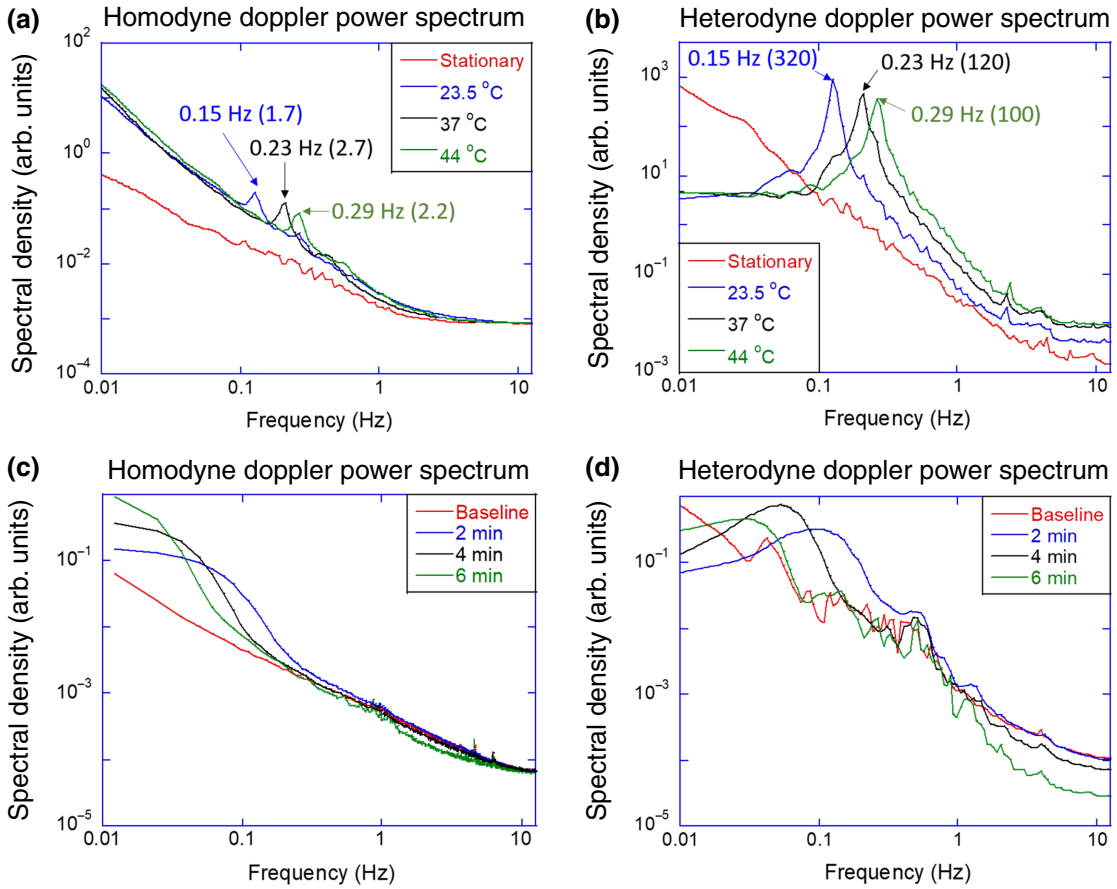

FIG. 2. Doppler signatures in fluctuation spectra. (a) Homodyne spectra of slowly moving paper with (b) associated heterodyne spectra. Numbers in parentheses are signal-to-background ratios. (c) Homodyne spectra of bacterial pellets responding to nutrient shock and (d) associated heterodyne spectra.

plotted. The heterodyne power spectra show clear peaks at 0.15, 0.23, and 0.29 Hz, which correspond to speeds of 50, 77, and 97 nm/s, respectively, at the three different temperatures. In contrast, the homodyne spectrum shows only a "residual" Doppler peak that is caused by the small number of holographic fringes (approximately three) per speckle on the camera plane. As a fringe drifts out of a speckle, the average intensity is modulated, which appears as a small intensity modulation peak in the homodyne spectrum.

To compare the characteristics of homodyne and heterodyne power spectra of a biological system that has directed motion, we investigate a bacterial pellet that responds to nutrient shock. Homodyne and heterodyne power spectra of bacterial chemotaxis-induced dynamics are shown in Figs. 2(c) and 2(d). The statistical characteristics of the bacterial dynamics are analyzed by measuring the Doppler edge frequency, which is caused by three-dimensional ballistic motion with long persistence times [5]. To measure the three-dimensional bacterial motions induced by chemotaxis, a dense *Escherichia coli* (*E. coli*) high-bacterial-density pellet (10^{10}colony-forming units/ml) is extracted from a culture medium (10^8 colony-forming units/ml) by centrifugation (15 000 rpm for 3 min). The pellets are dipped in 300 μl of 1% NaCl solution for 5 h to establish *E. coli* in the stationary phase. To induce nutrient shock and chemotaxis, 150 μl of the medium is removed and 150 μl of Lysogeny-broth (LB) medium is added. The Doppler spectra of *E. coli* pellets are measured by BDI before and after applying the LB medium, and 2048 holograms are recorded per measurement with a sampling frequency of 25 frames/s. The collective motion within the *E. coli* pellet after applying the LB medium is observed using the homodyne spectrum shown in Fig. 2(c). A prominent Doppler edge appears immediately after applying the LB medium, representing three-dimensional persistent motion [5]. The heterodyne spectrum, shown in Fig. 2(d), displays a broad Doppler peak, but with considerably less stability. The frequency of the maximum spectral density enhancement by nutrient shock reflects the Doppler frequency of the persistent motion, which is related to the average speed of the bacterial motion along the vertical direction as

$$\Delta\omega_D = \mathbf{q}\cdot\mathbf{v}. \tag{3}$$

As shown in Fig. 2(b), heterodyne detection on the slowly moving paper clearly has better sensitivity to directed motion than that of the homodyne. However, the higher sensitivity becomes a disadvantage if phase stabilization of the measurement system is not optimal. The stability of spectral changes shown in Figs. 2(c) and 2(d) demonstrates the disadvantage of heterodyne detection in an unstabilized optical system.

IV. PHASE-STABILIZED DETECTION

The dynamic characteristics of random processes can be characterized in two extremes either as diffusive or ballistic. Biological processes have primarily ballistic characteristics due to active transport driven by molecular motors, intracellular undulations, cell crawling, etc., with long persistence times [32]. Doppler shifts produced by scattering from biological systems carry the ballistic phase displacements. However, the phases of scattered photons also carry random phase excursions caused by external mechanical perturbations, diffusive background, and optical phase decoherence from multiple scattering [33].

As an alternative to the physical stabilization of the optical system, it is possible to perform digital postprocessing to stabilize the phase by constructing low-noise probability distribution functions (Φ_{PDF}) of short-time phase excursions. Ballistic motions have persistent lengths and times, and the time evolution of Φ_{PDF} contains both persistent phase displacements and phase diffusion. Persistent phase displacement defines the maximum likelihood of Φ_{PDF}, while phase noise defines the variance. Systems with diffusive characteristics, relative to ballistic, induce different speckle statistics [32], and histograms of the phases of the complex-value reconstructed speckle from experimental data capture the phase-displacement statistics.

A. Phase displacements and Φ_{PDF}

Reconstructed dynamic speckle at the FP produces a functional (time-dependent) image that contains Doppler information in the form of a distribution of multiwave beat frequencies. The phase of reconstructed holograms is limited to values between $-\pi$ and $+\pi$, and the phase time series drifts through slow drift of the physical system. Therefore, an alternative approach finds the drifting phase of individual pixels within specified times and constructs a Φ_{PDF} of phase displacements.

The phase of randomly interfering photons can be described as

$$Ae^{i\phi_{tot}} = \sum_{n=1}^{N} e^{i\phi_n}, \tag{4}$$

where A is the amplitude after vector summation. A photon with wave vector $\mathbf{q}$ scatters from a scattering element at $\mathbf{r}$ contributing to the phase angle and is assumed to have isotropic orientation. The average Doppler shift can be expressed as

$$\phi_{\mathrm{tot}}(\boldsymbol{r}, t) = \phi_{\mathrm{geo}} + \sum_{i=1}^{N} \mathbf{q}(\mathbf{r}_i) \cdot \mathbf{v}_i t, \tag{5}$$

where Φ_{geo} is a global phase angle determined by geometric factors. The geometric contribution is quasistatic when we assume the distribution of the scattering elements does not change rapidly. On the other hand, the Doppler-frequency-shift contribution to phase is on the time term, so the time derivative of $\Phi_{\mathrm{tot}}(\mathbf{r},t)$ contains the total contribution from all partial-wave Doppler shifts. As a result, the time-averaged total Doppler shifts contributing to speckle phase can be defined as

$$\Delta\overline{\phi}(\mathbf{r}, \tau) = \int_0^{\tau} \frac{\partial \phi(\mathbf{r}, t)}{\partial t} dt. \tag{6}$$

To avoid the phase-wrapping problem, the phase displacements are acquired by $e^{i\Delta\phi} = e^{i(\phi_f - \phi_i)}$ between consecutive reconstructed holograms. The phase angle $\Delta\phi$ is obtained from the values of the real and imaginary parts, and a minimum angle is chosen to avoid phase wrappings. The phase time series $\phi(\mathbf{r}, \tau)$ of the functional images are reconstructed by adding $\Delta\overline{\phi}(\mathbf{r}, \tau)$ to the previous frame and allowing the phase excursions to extend beyond $\pm\pi$ by using

$$\phi_{xy}(t_{n+1}) = \phi_{xy}(t_n) + \Delta\phi_{xy}(t_n), \tag{7}$$

where $\phi_{xy}(t_n)$ is the absolute phase at time t_n, and $\Delta\phi_{xy}(t_n)$ is the phase excursion from time t_{n+1} to time t_n. The phase difference from Eqs. (4) and (5) is

$$\frac{\Delta\phi}{\Delta t} = \sum_{i=1}^{N} \mathbf{q}_i \cdot \boldsymbol{v}_i = \vec{q} \cdot \vec{v}_{\mathrm{drift}}. \tag{8}$$

The averaged phase displacement $\Delta\overline{\phi}$ derived from Φ_{PDF} is related to the average persistence length $\Delta\bar{x}$ of the dynamic particles. When external noise contributes to Φ_{PDF}, it contributes to the width, but does not affect the average phase displacement $\Delta\overline{\phi}$. For instance, mechanical vibrations or optical source noise can perturb the average $\Delta\overline{\phi}$ between two consecutive frames, but the effect vanishes by taking a time average over many frames due to the zero-mean-noise characteristic.

The Gaussian-approximated behavior of Φ_{PDF} is given by

$$\Phi_{\mathrm{PDF}}(\Delta\phi, \Delta t) = \frac{1}{\sqrt{4\pi D_\phi \Delta t}} \exp\left(-\frac{(\Delta\phi - \langle\vec{q}\cdot\vec{v}\rangle\,\Delta t)^2}{4D_\phi \Delta t}\right), \tag{9}$$

with mean and variance $\Delta\bar{\phi} = \langle\vec{q}\cdot\vec{v}\rangle\,\Delta t$ and $\langle\Delta\phi\rangle^2 = 2D_\phi\Delta t$, where D_ϕ is a one-dimensional diffusion constant. The phase excursions depend only on the single axial dimension defined by the backscatter direction. The phase diffusion constant from stationary paper and paper on the evaporating water surface at temperatures of 23.5, 37, and 44 °C are 0.005, 0.02, 0.015, and 0.02 rad^2/s, respectively. The phase diffusion constants of biological systems, such as DLD-1 tumor spheroids and *E. coli* pellets, are much larger at 0.1 rad^2/s (DLD-1), 0.13 rad^2/s (pellet without nutrient), and 0.15 rad^2/s (pellet with nutrient).

B. Calibration with macroscopic directed motion

To obtain Φ_{PDF} from functional speckle imaging, the statistical phase displacements of the functional images from the experiment conducted in Fig. 1 are acquired. A phase-displacement distribution is acquired by subtracting two frames with time interval τ, and the normalized histogram of the phase displacement represents the probability density function. The Φ_{PDF} of the phase displacement of time interval τ with N hologram time series is

$$\Phi_{\mathrm{PDF}}[\Delta\phi(\tau)] = \frac{1}{N}\sum_{t_i=1}^{N-\tau}\sum_{j=1}^{(x,y)} \mathrm{histogram}[\phi(\mathbf{r}_j, t_{i+\tau}) - \phi(\mathbf{r}_j, t_i)] \tag{10}$$

The statistics are collected over the dynamic speckle of each pixel, and the spatial information (x and y) is lost during this procedure. Alternatively, subregions can be defined in the field of view over which Φ_{PDF} is constructed to create tissue-scale maps of the speckle statistics, as in speckle contrast imaging [34].

The temporal evolution of Φ_{PDF} is shown in Figs. 3(a) and 3(b). The vertically moving paper target has persistent motion, and the optical measurement captures the Doppler signal caused by the vertical dynamics and background noise. Here, the Doppler slope is defined as an averaged phase displacement per time delay τ, which can be obtained by

$$\frac{\Delta\bar{\phi}}{\tau} = \frac{1}{\tau}\sum_{\Delta\phi=-\pi}^{\pi} \delta\phi \times \Phi_{\mathrm{PDF}}(\Delta\phi) \tag{11}$$

The sign of the phase is set to be positive for upward and negative for downward motion, so the Φ_{PDF} with different τ in Fig. 3(b) shows the negative Doppler slope in Fig. 3(c). All Φ_{PDF} amplitudes shown in Fig. 3(a) decrease

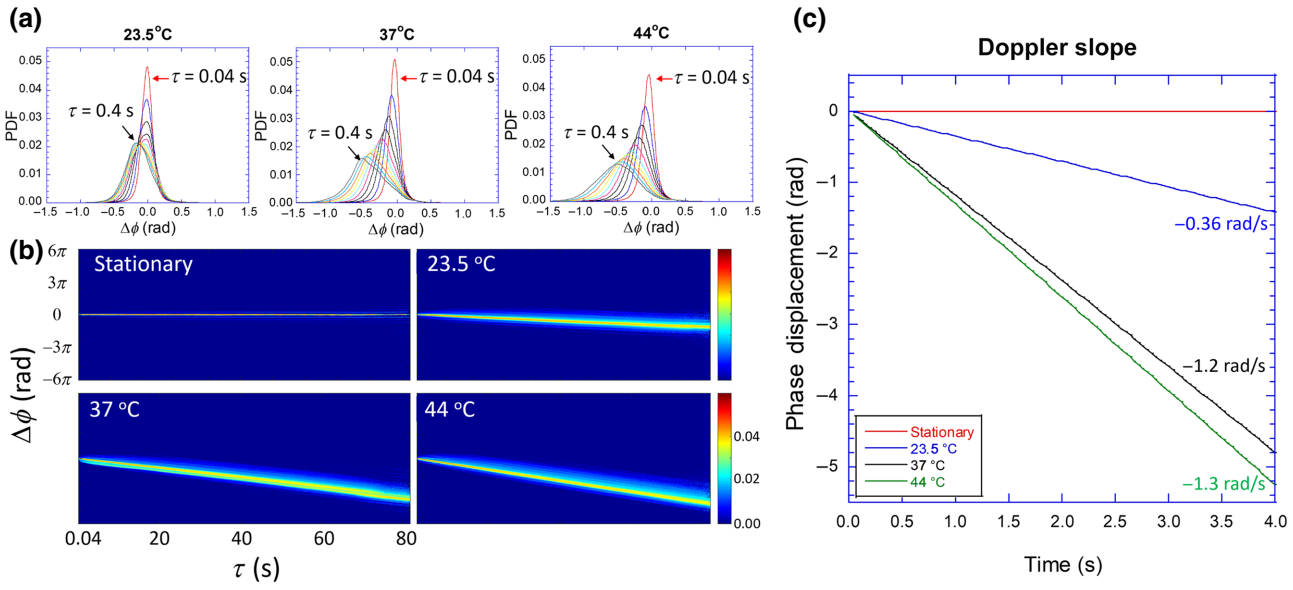

FIG. 3. Doppler information acquisition from functional speckle imaging. (a) Temporal evolution of Φ_{PDF} and (b) two-dimensional plot of Φ_{PDF} evolving over time. (c) Average phase displacements and corresponding Doppler slopes at temperatures of 23.5, 37, and 44 °C. Induced phase shifts are −0.93, −1.38, and −1.88 rad/s, which correspond to Doppler shifts of 0.15, 0.22, and 0.30 Hz, and speeds of 50, 70, and 100 nm/s, respectively. Doppler slopes derived from Φ_{PDF} show good agreement with the heterodyne peaks in Fig. 2(b).

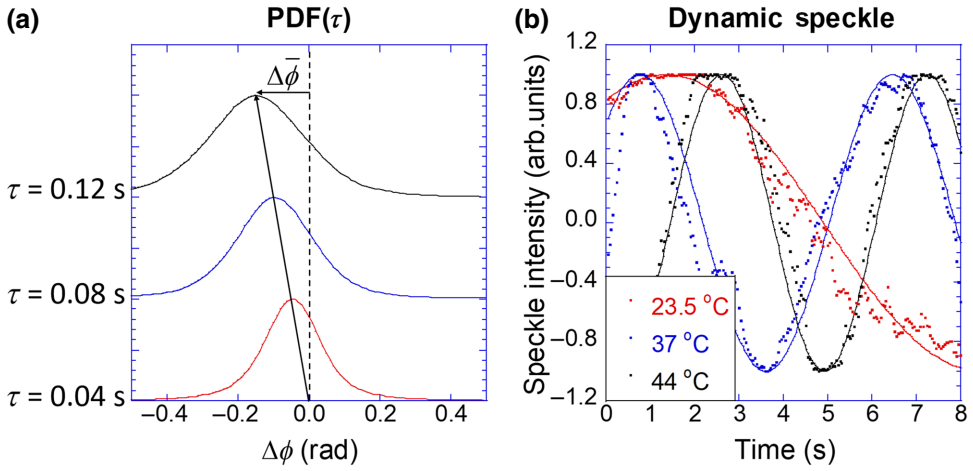

FIG. 4. (a) Time evolution of Doppler Φ_{PDF} shows stable distributions, but momentary phase displacements can drift randomly. (b) Experimentally acquired amplitude-normalized fluctuation (dots) of dynamic speckle and modulation (solid lines).

and the widths increase as a function of delay because of optical decoherence [35].

The time-averaged speed of the slowly moving paper can be estimated from $\Delta\bar{\phi}$. The speeds of the target at different temperatures are estimated to be 17, 63, and 67 nm/s, which are consistent with the power spectral Doppler peak frequency in Fig. 2(b). Φ_{PDF} shows a stable time dependence in Fig. 4(a), but the actual dynamic speckle amplitudes show sinusoidal behavior with minor random fluctuations [Fig. 4(b)]. The temporal Fourier transform of dynamic speckle fluctuations tends to be noisy due to minor random fluctuations. However, the average phase displacements obtained from Φ_{PDF} provide a good estimate of the average Doppler shift and the power spectral density. For instance, the average phase displacement of the evaporating water surface has a linear phase displacement and the dynamic speckle has a sinusoidal amplitude modulation caused by the Doppler beat frequency. Sinusoidal functions estimated from the average phase displacements from Φ_{PDF}, and shown in Fig. 4(b) as solid curves, have smoother temporal behavior than that of the direct experimental measurements.

C. Φ_{PDF} of bacterial dynamics induced by nutrient shock

The nutrient shock of bacterial pellets, inducing chemotaxis, shows prominent Doppler edges in the homodyne spectra in Fig. 2(a). The same method as that used for obtaining Φ_{PDF} in Fig. 3 is used to obtain the chemotaxis Φ_{PDF} of the *E. coli* pellets. The time evolution of Φ_{PDF} shows nonzero phase displacement immediately after adding a nutrient. Equal volumes (150 μl) of reagents are added to the wells as the medium is removed and readded to the same well to test the pipetting-perturbation effect, and 1% and 7% NaCl media are used to verify the effect of applying medium without nutrients and to test the osmotic pressure of the LB medium without nutrients.

The sign of the phase is calibrated by the measurement of the Doppler shifts at the water surface from Fig. 3 and set a positive direction for upward and negative direction for downward. The baselines are measured 3 times for 6 min, while the *E. coli* pellet is in a stationary state. After applying reagents, responses are measured 13 times for 26 min. The temporal evolution of Φ_{PDF} immediately after applying reagents are shown in Figs. 5(a) and 5(b). The average Doppler slopes from each measurement are shown in Fig. 5(c). The average Doppler slope shows an immediate response after applying reagents and then decays exponentially. The temporal decay coefficients α and amplitudes of the average Doppler slopes are shown in Fig. 5(c) and summarized in Table I. The Doppler slope measurements on *E. coli* pellets after applying various reagents show a range of characteristics. For instance, the LB medium induces pellet expansion, while 7% NaCl induces shrinkage of the bacterial pellets. The expansion under LB medium can be explained in terms of increased activity of the bacterial cells, while the contraction under 7% salt is caused by the high external osmolarity that induces partial desiccation of the cells. Applying 1% NaCl solutions shows the slowest speed (2.6 nm/s). Applying 7% NaCl solutions induces a net motion in the negative direction (downward) with the fastest speed (15.4 nm/s). The motions of *E. coli* induced by 1% and 7% NaCl solutions show similar decay coefficients. The LB medium induces an intermediate speed, and the motion lasts about twice as long as applying NaCl solution. The pipetting perturbation of the *E. coli* pellet is not measurable.

D. Stabilized heterodyne Doppler spectrum

The time evolution of a Φ_{PDF} is equivalent to the temporal autocorrelation of the Doppler shift. The experimentally obtained Φ_{PDF} is stable due to suppressing random phase noise, while maintaining the Doppler shift. Therefore, the reconstruction of the heterodyne power spectral density from Φ_{PDF} should have a more stable Doppler

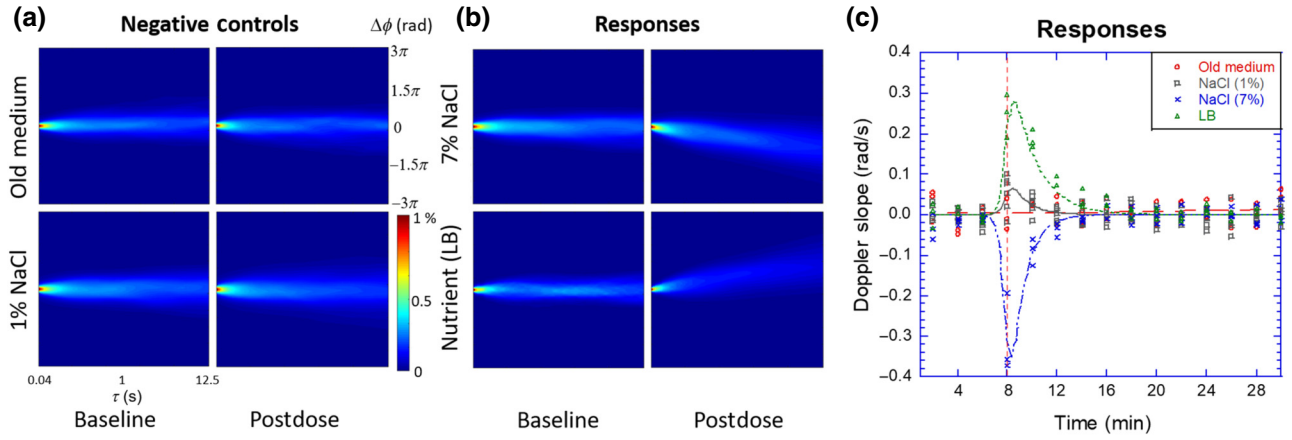

FIG. 5. Temporal evolution of Φ_{PDF} of *E. coli* pellets showing Doppler slopes. (a) Temporal response of Φ_{PDF} immediately after applying negative-control reagents (perturbing medium with a pipette and adding 1% NaCl medium) and (b) high-osmotic-pressure solution (7% NaCl) and nutrient (LB). (c) Doppler slopes from Φ_{PDF}. Applying medium (pipetting perturbation) and 1% NaCl solution (LB medium base without nutrient compound) does not induce significant shifts. 7% NaCl (osmotic shock) and LB (nutrient shock) media show shifts of Φ_{PDF} with opposite signs.

spectral density than that obtained from the heterodyne time series. The autocorrelation (AC) of a field with a time interval τ can be estimated from Φ_{PDF} by calculating the expectation value of $e^{i\Delta\phi}$ which can be denoted as

$$A(\tau) = E^2 \sum_{\Delta\phi} \Phi_{\mathrm{PDF}}[\Delta\phi(\tau)] e^{i\Delta\phi(\tau)} \tag{12}$$

by assuming the field amplitude varies more slowly than the phase displacement $\Delta\phi(\tau)$. The refined heterodyne power spectrum of the signal from Φ_{PDF} can be obtained by performing a Fourier transform on $A(\tau)$ by the Wiener-Khinchin theorem:

$$S_{\mathrm{het}}(\omega) = \int A(\tau) e^{i\omega\tau} d\tau. \tag{13}$$

From the Φ_{PDF} of the water-surface target paper [Fig. 3(a)] and the *E. coli* pellet, the AC and the corresponding refined heterodyne power spectra are obtained and are shown in Fig. 6. The Fourier transform of the autocorrelation has a limited time window due to the limited sampling bandwidth (0.02 Hz–12.5 Hz). The sampling time window is 80 s and the autocorrelation shown in Fig. 6(a) has a limited time window from −40 to 40 s. The heterodyne Doppler power spectrum of the paper target on the evaporating water surface shows about 10 times enhanced detection sensitivity of the Doppler peak, relative to the conventional heterodyne power spectrum in Fig. 2(b), by suppressing the phase noise by constructing Φ_{PDF}. The raw heterodyne power spectrum of the bacterial pellets in Fig. 2(d) is not stable, but the refined heterodyne power spectra derived from Φ_{PDF} shows prominent Doppler features in Fig. 6(d). The homodyne spectrum is always symmetric, which means the spectrum cannot distinguish the sign of the dynamics, but the refined heterodyne power spectrum shows well-characterized heterodyne power spectral enhancement, including the sign of the dynamics.

TABLE I. Response characteristics of bacterial pellets to different reagents.

Reagent	α (t^{-1})	Maximum doppler slope amplitude (rad/s)	Average velocity (nm/s)
Old medium	NA	NA	NA
NaCl (1%)	0.53 ± 0.41	0.05 ± 0.04	2.6 ± 2.2
NaCl (7%)	0.59 ± 0.06	-0.31 ± 0.1	-15.4 ± 5
LB	0.26 ± 0.06	0.25 ± 0.05	13 ± 3

V. LEVY-STABLE DISTRIBUTIONS

The dynamics of light-scattering elements may have anomalous occasional ballistic motions [36–38] that cause large random phase excursions with low probability, which can form power-law tails in the Φ_{PDF}. For instance, the probability in the tail may behave as [39]

$$P(|x|) \propto \frac{1}{|x|^{1+\alpha}}. \tag{14}$$

Such distributions are said to have *heavy tails* because the probability falls more slowly than exponentially for large arguments. Heavy tails on a distribution cause rare but high-amplitude events that are referred to as outliers and sometimes as "black swans" [40]. These events are fundamentally part of the distribution and are not anomalies, but can have a disproportionate effect when attempting to calculate variances or even mean values. For instance, there is

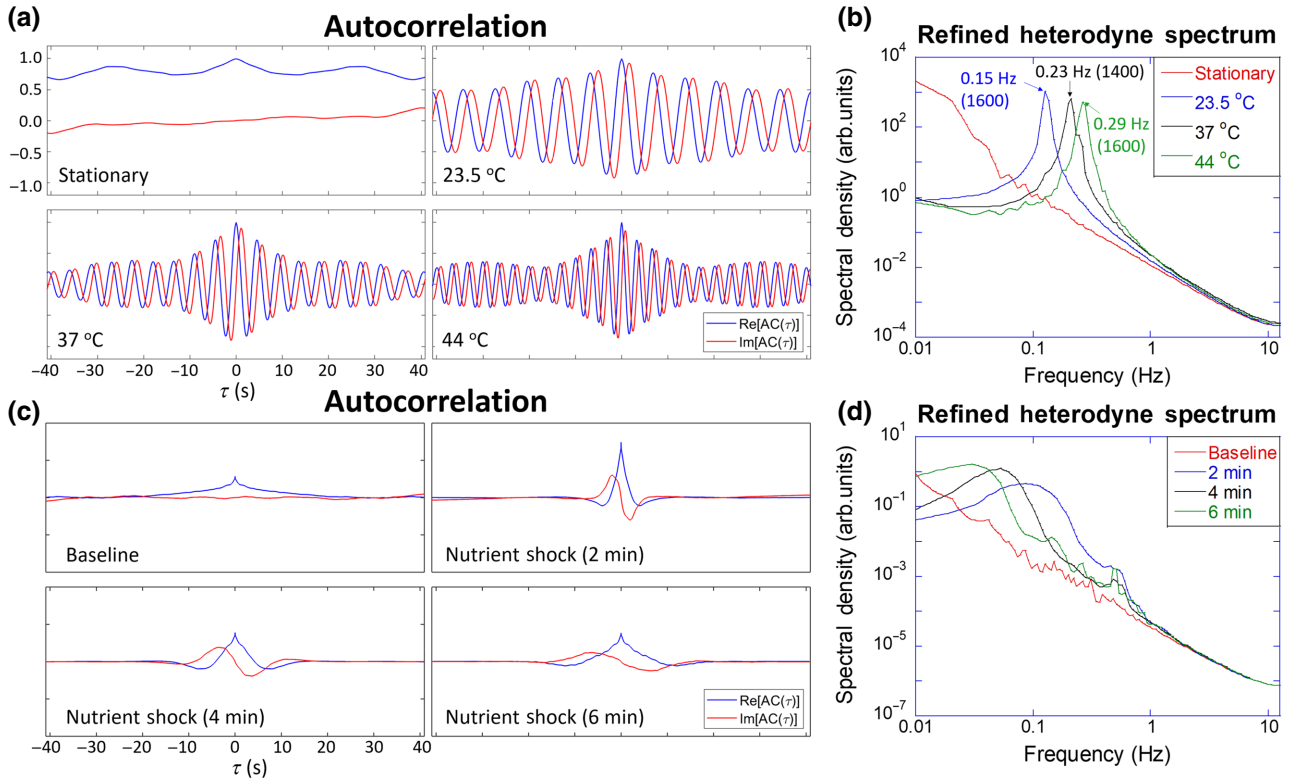

FIG. 6. (a) ACs of Doppler shift induced by water-surface evaporation speed obtained from Fig. 3(a) by Eq. (12) at different temperatures. AC of negative time is the complex conjugate of positive time, so the real-value AC is symmetric and the imaginary-value AC is asymmetric. (b) Power spectrum derived from the complex autocorrelation by the Weiner-Khinchin theorem. Signal-to-background ratios (numbers in parentheses) of the refined heterodyne Doppler peaks are 10 times more sensitive than the raw heterodyne power spectra of Fig. 2(b). (c) AC of Doppler shift of *E. coli* pellet under nutrient shock. (d) Reconstructed heterodyne power spectrum from AC.

a large class of probability distributions for which the variance and high-order moments diverge. A subset of such distributions includes so-called stable distributions.

In probability theory, a distribution is called *stable* if the sum of two independent random variables that come from the distribution have the same distribution. The normal (Gaussian) distribution has this property because the sum of two normally distributed independent variables is also normally distributed. The variance and possibly the mean may be different, but the functional form is still Gaussian. The general form of a probability distribution can be obtained by taking a Fourier transform as

$$P(x) = \frac{1}{2\pi}\int_{-\infty}^{\infty} \varphi(k) e^{-ikx} dk, \tag{15}$$

where $\varphi(k)$ is known as the *characteristic function* of the probability distribution. A special case of a stable distribution is the Levy-symmetric stable distribution obtained as [39]

$$P_{\alpha,\gamma}(x) = \frac{1}{\pi}\int_{0}^{\infty} e^{-\gamma q^{\alpha}} \cos(qx) dq \tag{16}$$

and characterized by the parameters α and γ. The characteristic function, in this case, is a stretched exponential. The Levy distribution has a power-law tail at large values, given by Eq. (14), but for smaller values has a characteristic length scale set by the parameter γ. The special case of the Levy distribution for $\alpha = 2$ is a normal distribution. The special case of the Levy distribution for $\alpha = 1$ is the Cauchy distribution given by

$$P_{1,\gamma}(x) = \frac{1}{\pi}\frac{\gamma}{\gamma^2 + x^2}. \tag{17}$$

The Cauchy distribution is normalizable (probabilities integrate to unity) and has a characteristic scale set by γ, but it has a divergent mean value, violating the central limit theorem. For distributions that satisfy the central limit theorem, increasing the number of samples from the distribution allows the mean value to converge on a finite value. For the Cauchy distribution, on the other hand, increasing the number of samples increases the chances of obtaining a black swan, which skews the mean to larger values, as it diverges in the limit of an infinite number of samples.

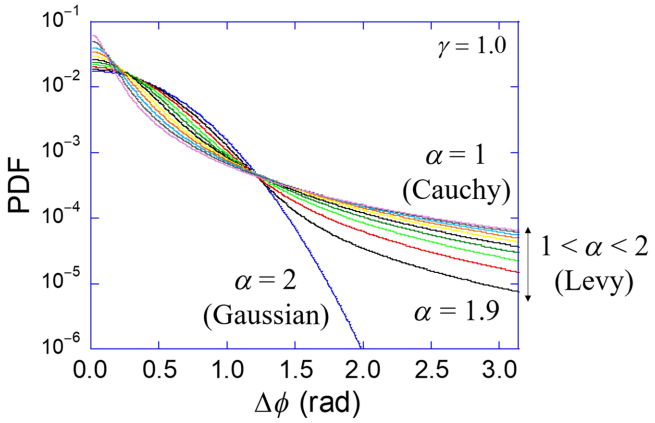

FIG. 7. Levy-stable probability distribution functions between $\alpha = 1$ (Cauchy) and $\alpha = 2$ (Gaussian). Heavy tail is seen, even for $\alpha = 1.9$ close to the Gaussian case.

Examples of Levy-stable probability distribution functions are shown in Fig. 7 for a range between $\alpha = 1$ (Cauchy) and $\alpha = 2$ (Gaussian). The heavy tail is seen, even for the case $\alpha = 1.9$ close to the Gaussian distribution. In the case of the Gaussian distribution, the mean-squared displacement is finite. However, for all other cases, the mean-squared displacement is divergent, which is caused by the large path lengths that become more probable as α approaches unity.

Stable distributions with divergent moments play important roles in biology. For instance, a random walk with a Levy distribution of path lengths, known as a Levy walk, can be an efficient means for an organism to search for food [38,41]. They can also participate in intracellular transport processes. Waiting times can have stable distributions and path lengths. The sampling of these processes from stable probability distributions is one way that anomalous transport emerges in intracellular motion.

VI. LEVY SPECTROSCOPY

As a demonstration of the utility of phase-sensitive Doppler fluctuation spectroscopy, we use the technique to perform an initial study of the occurrence of anomalous phase excursions that occur in living systems. The Φ_{PDF} represents the statistical characteristics of the random processes associated with light-scattering elements. The phase displacements have a one-to-one correspondence to the displacements $\Delta\bar{x}$ of the scattering elements by Eq. (8). Therefore, fitting the shape of the Φ_{PDF} with the Levy distribution of Eq. (16) may help to display the anomalous ballistic characteristics of intracellular and bacterial scattering elements. To reduce the external phase noise contribution to the shape of the Φ_{PDF}, the smallest sampling window, τ_{min}, is used to analyze the statistical characteristics of the Φ_{PDF} (τ_{min}). Analysis of the power-law tails requires a large sample size because the characteristics of power-law tails depend on the decaying tendency of rare probabilities. The size of the functional image is about 10^4 pixels and the images are recorded for more than 2000 frames. Therefore, the statistics of Φ_{PDF} are established on about 10^7 samples of experimental measurements. The phase spanned from $-\pi$ to π rad with a resolution of 0.01 rad.

A. Levy-like characteristics of Φ_{PDF}

Calibration experiments are analyzed by Levy-alpha spectroscopy. The Levy fits of Φ_{PDF} of the stationary paper, sinking paper, tumor spheroids, and$\Delta\phi$ *E. coli* pellets are shown in Fig. 8. The Φ_{PDF} of stationary paper shows a Levy alpha close to two, which represents the Gaussian phase noise of the optical source [35]. The moving paper from Fig. 1(c) shows a slightly decreased alpha contributed to by mechanical motion, but the alpha is still close to two. Biological objects, such as tumor spheroids and an *E. coli* pellet, show a Levy alpha of less than 1.6, which are more Cauchy-like and may be related to ballistic random walks observed in biological systems [36–38].

B. Levy spectroscopy of bacterial infection of epithelial tissue

Foodborne pathogens have various infection mechanisms. For instance, *Listeria monocytogenes* (*L. monocytogenes*) target epithelial cells and infiltrate host cells by physically penetrating cell walls. After internalization, *L. monocytogenes* synthesizes actin tails by using host-cell resources to gain a propulsion force toward neighboring host cells [25,42]. The spreading infection goes beyond diffusion [25], and the spreading speed may be governed by rare outliers, which is a key characteristic of Levy walks. On the other hand, *Listeria innocua* (*L. innocua*) are from the same *Listeria* genus, but *L. innocua* do not have an effective infection mechanism [43]. The interaction of *L. innocua* with host cells is passive and opportunistic compared to *L. monocytogenes* [44].

L. monocytogenes and *L. innocua* are cultured in LB medium for 24 and 48 h, respectively, at 37 °C to reach 10^8 colony-forming units/ml. For host-cell preparation, DLD-1 (epithelial adenocarcinoma cell line) is selected because it can grow to have three-dimensional tissue characteristics and a loose cellular structure for observing rapidly spreading infection.

The seed cells (American Type Culture Collection) are cultured in RPMI-1640 medium with 25 mM HEPES buffer (Gibco), 10% fetal bovine serum (Atlanta Biologicals), and antibiotics (100 U/ml penicillin and 100 μg/ml streptomycin) for 4–5 days. When DLD-1 multicellular spheroid structures formed, they are transferred to a 96-well BioCoat plate (Corning) with an antibiotic-free RPMI-1640 medium (300 μl/well). After DLD-1

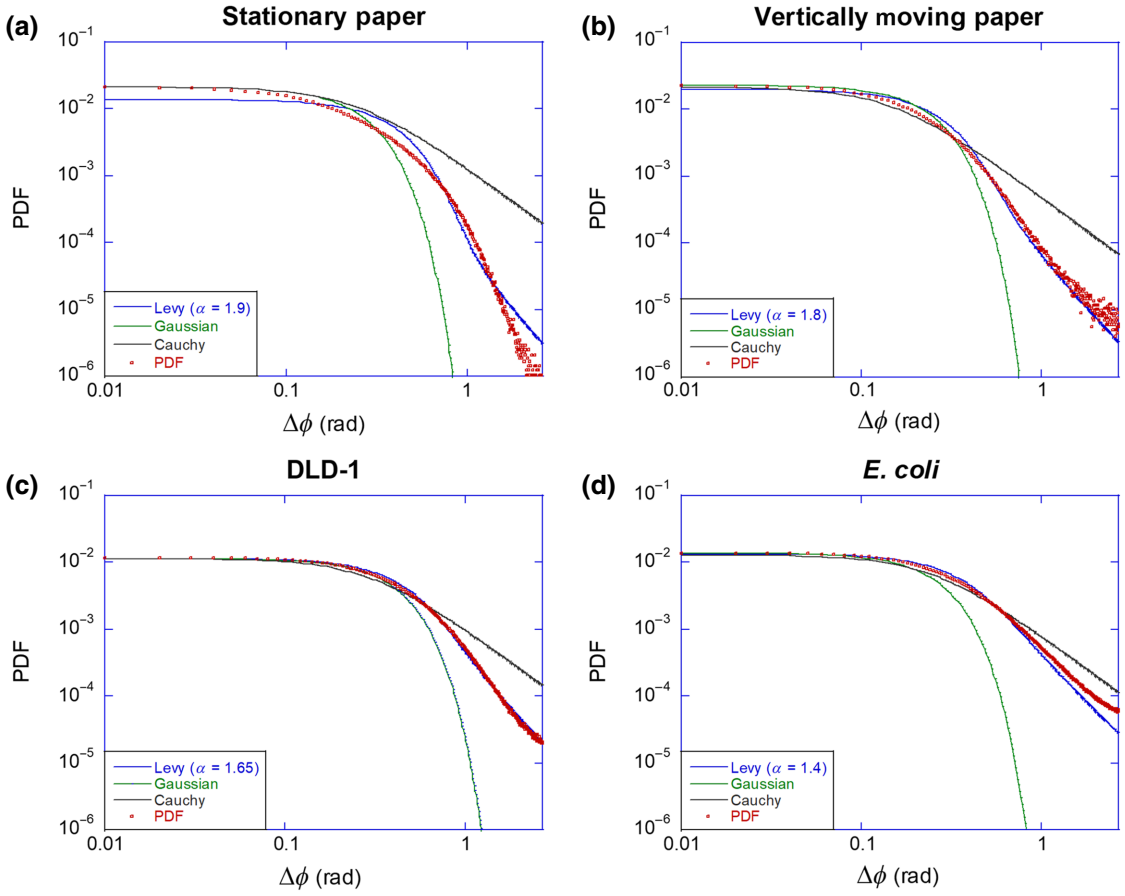

FIG. 8. Φ_{PDF} of various targets fitted with Levy, Gaussian, and Cauchy distributions of (a) stationary paper, (b) vertically moving paper by water-surface evaporation, (c) DLD-1 spheroids, and (d) *E. coli* pellet. Cauchy probability density shows power-law tails with $\alpha = 1$ (black solid lines) and Gaussian probability density with $\alpha = 2$ (green solid lines). Levy distributions show similar heavy tails of experimentally obtained Φ_{PDF}. Power-law tails of Levy-probability densities are numerically obtained and fitted with the smallest residual squares. To verify the slopes of the power-law tails, maximum likelihoods of Φ_{PDF} are shifted to $\Delta\Phi = 0$ to be plotted symmetrically.

transfer, the media are refreshed with RPMI-1640 without antibiotics.

An infection assay using DLD-1 spheroids [45] is analyzed using Levy-alpha spectroscopy of Φ_{PDF}. Interaction between bacteria and DLD-1 should change the statistical characteristics of scattering elements due to the inoculated bacterial dynamics. Also, the different strategic behavior of *L. monocytogenes* relative to that of *L. innocua* is expected to produce different Φ_{PDF} changes, where *L. monocytogenes* actively interacts with DLD-1 host cells and shows more ballistic behavior. Before applying bacteria to DLD-1, three baselines are measured for 90 min. After the baselines are established, 10^7 colony-forming units of *L. monocytogenes* or *L. innocua* are inoculated for the infection cohort and growth medium is used for the control cohort. The dynamic speckle of the two cohorts are measured for 6 h. The Φ_{PDF} of each DLD-1 spheroid is obtained to compare the Levy-alpha values of baselines and infection measurements. The initial Levy-alpha values can vary due to DLD-1 characteristics, and three Levy-alpha values of baseline measurements are averaged. After inoculation, the shifts of Levy-alpha values are obtained. The group inoculated with *L. monocytogenes* shows significantly decreased alpha values (heavier tails with more outliers), while *L. innocua* shows only a small change. The Φ_{PDF} of DLD-1 before and after infection are compared in Figs. 9(a) and 9(b). Decreased alpha values suggest that the mechanical behavior of random processes becomes more Cauchy-like (ballistic) than Gaussian-like (diffusive) after inoculation with the pathogenic bacteria.

The Levy-alpha shifts are shown in Fig. 9(c). Baselines of all cohorts show a stable distribution and the variance of Levy-alpha values shows almost identical overlap with the control. Inoculation by *L. monocytogenes* and *L. innocua* shows negative shifts in alpha due to bacterial dynamics. The baselines are measured for 90 min. The

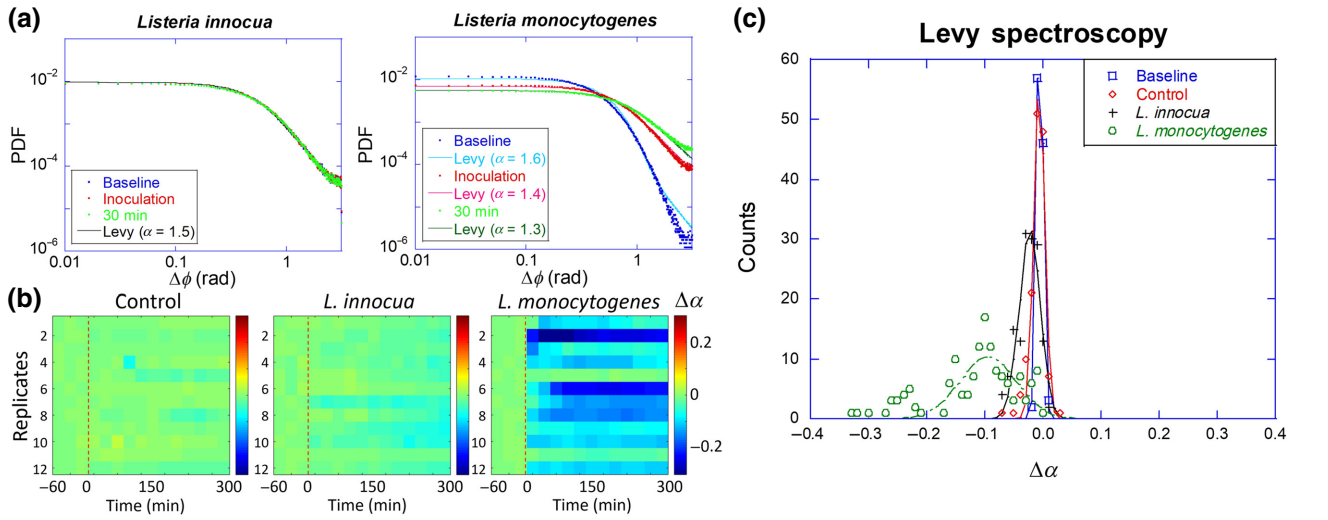

FIG. 9. Levy-alpha spectroscopy infection assays. Two bacterial strains with the same genus (*Listeria*) with different pathogenicities (*innocua* and *monocytogenes*) are inoculated into living DLD-1 tumor spheroids. (a) Examples of Φ_{PDF} and Levy distributions. Nonpathogenic *L. innocua* induces a slight change in Levy alpha, while pathogenic *L. monocytogenes* significantly decreases Levy alpha. (b) Statistical analysis of Levy-alpha value changes ($\Delta\alpha$) of 12 replicates. 10^7 colony-forming units of bacteria are inoculated at 0 min (red-dashed line) and the Φ_{PDF} are measured for 6 h. Levy-alpha changes to control and *L. innocua* infection groups show comparable small variations, while *L. monocytogenes* shows a significant decrease in alpha. (c) Histogram of Levy-alpha spectroscopy collected from (b). Invasive *L. monocytogenes* induces Levy-alpha shifts, while passive *L. innocua* shows only a minor shift of the average Levy-alpha value. Control and baselines show almost identical statistical behavior. Lines are fitted Gaussian distributions.

control also shows a stable distribution over a 6-h measurement. *L. monocytogenes* shows the largest difference due to the characteristics of the infection. The range of Levy-alpha values may be because the scanned area of DLD-1 may have fully infected regions, partially infected regions, or regions isolated from infection, producing variations.

VII. CONCLUSIONS

Phase-sensitive detection of Doppler shifts by dynamic light scatting is demonstrated. Comparisons between the calibration experiments and the phase-sensitive detection method show good agreement and improved stability compared with the conventional heterodyne detection method. By introducing statistical averaging on the time-delayed phase displacements, the random phase noise can be canceled, while the net Doppler shift caused by ballistic motions remains detectable, which improves the detection sensitivity. Furthermore, the probabilistic analysis of the phase displacement in biological systems shows an anomalous ballistic distribution that is close to the Levy distribution. The Levy-alpha values of Φ_{PDF} are obtained numerically and shifts of the Levy-alpha values caused by bacterial infection are measured. Invasive bacterial infection of DLD-1 shows significantly decreased Levy-alpha values (heavier tail), while the control group and the group inoculated by noninvasive bacteria show only a slight change in alpha.

ACKNOWLEDGMENTS

This work is supported by NSF-CBET Grant No. 1911357.

[1] D. Huang, et al., Optical coherence tomography, Science **254**, 4 (1991).
[2] A. Dufour, V. Shinin, S. Tajbakhsh, N. Guillén-Aghion, and O.-M. Jean-Christophe, Segmenting and tracking fluorescent cells in dynamic 3-D microscopy with coupled active surfaces, IEEE Trans. Image Process. **14**, 1396 (2005).
[3] B. J. Berne and R. Pecora, *Dynamic Light Scattering: with Applications to Chemistry, Biology, and Physics* (Dover, Mineola, New York, 2000).
[4] P. Yu, L. Peng, M. Mustata, J. J. Turek, M. R. Melloch, and D. D. Nolte, Time-dependent speckle in holographic optical coherence imaging and the state of health of tumor tissue, Opt. Lett. **29**, 68 (2004).
[5] W. Tan, A. L. Oldenburg, J. J. Norman, T. A. Desai, and S. A. Boppart, Optical coherence tomography of cell dynamics in three-dimensional tissue models, Opt. Express **14**, 7159 (2006).
[6] K. Jeong, J. J. Turek, and D. D. Nolte, Volumetric motility-contrast imaging of tissue response to cytoskeletal anti-cancer drugs, Opt. Express **15**, 14057 (2007).
[7] K. Jeong, J. J. Turek, and D. D. Nolte, Speckle fluctuation spectroscopy of intracellular motion in living tissue using coherence-domain digital holography, J. Biomed. Opt. **15**, 030514 (2010).

[8] D. D. Nolte, R. An, J. Turek, and K. Jeong, Holographic tissue dynamics spectroscopy, J. Biomed. Opt. **16**, 087004 (2011).
[9] D. D. Nolte, R. An, J. Turek, and K. Jeong, Tissue dynamics spectroscopy for three-dimensional tissue-based drug screening, J. Lab. Autom. **16**, 431 (2011).
[10] D. D. Nolte, R. An, J. Turek, and K. Jeong, Tissue dynamics spectroscopy for phenotypic profiling of drug effects in three-dimensional culture, Biomed. Opt. Express **3**, 2825 (2012).
[11] C. Joo, C. L. Evans, T. Stepinac, T. Hasan, and J. F. de Boer, Diffusive and directional intracellular dynamics measured by field-based dynamic light scattering, Opt. Express **18**, 2858 (2010).
[12] J. Kalkman, R. Sprik, and T. G. van Leeuwen, Path-Length-Resolved Diffusive Particle Dynamics in Spectral-Domain Optical Coherence Tomography, Phys. Rev. Lett. **105**, 198302 (2010).
[13] G. Farhat, A. Mariampillai, V. X. D. Yang, G. J. Czarnota, and M. C. Kolios, Detecting apoptosis using dynamic light scattering with optical coherence tomography, J. Biomed. Opt. **16**, 070505 (2011).
[14] J. Lee, W. C. Wu, J. Y. Jiang, B. Zhu, and D. A. Boas, Dynamic light scattering optical coherence tomography, Opt. Express **20**, 22262 (2012).
[15] A. L. Oldenburg, R. K. Chhetri, J. M. Cooper, W. C. Wu, M. A. Troester, and J. B. Tracy, Motility-, autocorrelation-, and polarization-sensitive optical coherence tomography discriminates cells and gold nanorods within 3D tissue cultures, Opt. Lett. **38**, 2923 (2013).
[16] C. Joo and J. F. de Boer, Field-based dynamic light scattering microscopy: Theory and numerical analysis, Appl. Opt. **52**, 7618 (2013).
[17] D. Merrill, H. Sun, J. Turek, D. Nolte, B. Yakubov, D. Matei, and R. An, Intracellular Doppler signatures of platinum sensitivity captured by biodynamic profiling in ovarian xenografts, Nat. Sci. Rep. **6**, 18821 (2016).
[18] C. Apelian, F. Harms, O. Thouvenin, and A. C. Boccara, Dynamic full field optical coherence tomography: Subcellular metabolic contrast revealed in tissues by interferometric signals temporal analysis, Biomed. Opt. Express **7**, 1511 (2016).
[19] C.-E. Leroux, F. Bertillot, O. Thouvenin, and A.-C. Boccara, Intracellular dynamics measurements with full field optical coherence tomography suggest hindering effect of actomyosin contractility on organelle transport, Biomed. Opt. Express **7**, 4501 (2016).
[20] H. Choi, Z. Li, H. Sun, D. Merrill, J. Turek, M. Childress, and D. Nolte, Biodynamic digital holography of chemoresistance in a pre-clinical trial of canine B-cell lymphoma, Biomed. Opt. Express **9**, 2214 (2018).
[21] Z. Li, R. An, W. M. Swetzig, M. Kanis, N. Nwani, J. Turek, D. Matei, and D. Nolte, Intracellular optical Doppler phenotypes of chemosensitivity in human epithelial ovarian cancer, Sci. Rep. **10**, 17354 (2020).
[22] M. A. Choma, M. V. Sarunic, C. H. Yang, and J. A. Izatt, Sensitivity advantage of swept source and Fourier domain optical coherence tomography, Opt. Express **11**, 2183 (2003).
[23] S. Tozburun, C. Blatter, M. Siddiqui, E. F. J. Meijer, and B. J. Vakoc, Phase-stable Doppler OCT at 19 MHz using a stretched-pulse mode-locked laser, Biomed. Opt. Express **9**, 952 (2018).
[24] J. F. de Boer, B. Cense, B. H. Park, M. C. Pierce, G. J. Tearney, and B. E. Bouma, Improved signal-to-noise ratio in spectral-domain compared with time-domain optical coherence tomography, Opt. Lett. **28**, 2067 (2003).
[25] F. E. Ortega, E. F. Koslover, and J. A. Theriot, Listeria monocytogenes cell-to-cell spread in epithelia is heterogeneous and dominated by rare pioneer bacteria, eLife **8**, 087004 (2019).
[26] W. Drexler and J. G. Fujimoto, *Optical Coherence Tomography: Technology and Applications* (Springer Berlin Heidelberg, 2008).
[27] D. D. Nolte, R. An, and J. Turek, in *Optical Coherence Tomography: Technology and Applications*, edited by J. G. Fujimoto and W. Drexler (Springer, Berlin, Heidelberg, New York, 2015), p. 1189.
[28] O. Thouvenin, K. Grieve, P. Xiao, C. Apelian, and A. C. Boccara, En face coherence microscopy, Biomed. Opt. Express **8**, 622 (2017).
[29] G. Indebetouw and P. Klysubun, Imaging through scattering media with depth resolution by use of low-coherence gating in spatiotemporal digital holography, Opt. Lett. **25**, 212 (2000).
[30] A. H. Meier and T. Roesgen, Heterodyne Doppler global velocimetry, Exp. Fluids **47**, 665 (2009).
[31] J. L. Monteith, Evaporation and environment, Symp. Soc. Exp. Biol. **19**, 205 (1965).
[32] Z. Li, H. Sun, J. J. Turek, S. Jalal, M. Childress, and D. D. Nolte, Doppler fluctuation spectroscopy of intracellular dynamics in living tissue, J. Opt. Soc. Am. A **36**, 665 (2019).
[33] A. Wax, C. H. Yang, R. R. Dasari, and M. S. Feld, Path-length-resolved dynamic light scattering: Modeling the transition from single to diffusive scattering, Appl. Opt. **40**, 4222 (2001).
[34] D. A. Boas and A. K. Dunn, Laser speckle contrast imaging in biomedical optics, J. Biomed. Opt. **15**, 011109 (2010).
[35] K. Kikuchi, Characterization of semiconductor-laser phase noise and estimation of bit-error rate performance with low-speed offline digital coherent receivers, Opt. Express **20**, 5291 (2012).
[36] F. Detcheverry, Generalized run-and-turn motions: From bacteria to Levy walks, Phys. Rev. E **96**, 012415 (2017).
[37] M. de Jager, F. J. Weissing, P. M. Herman, B. A. Nolet, and J. van de Koppel, Levy walks evolve through interaction between movement and environmental complexity, Science **332**, 1551 (2011).
[38] N. E. Humphries and D. W. Sims, Optimal foraging strategies: Levy walks balance searching and patch exploitation under a very broad range of conditions, J. Theor. Biol. **358**, 179 (2014).
[39] R. N. Mantegna, Fast, accurate algorithm for numerical simulation of Levy stable stochastic processes, Phys. Rev. E: Stat. Phys., Plasmas, Fluids, Relat. Interdiscip. Top. **49**, 4677 (1994).
[40] N. N. Taleb, *The Black Swan: the Impact of the Highly Improbable*, 1st ed. (Random House, New York, 2007).

[41] N. E. Humphries, H. Weimerskirch, N. Queiroz, E. J. Southall, and D. W. Sims, Foraging success of biological Levy flights recorded in situ, Proc. Natl. Acad. Sci. U. S. A. **109**, 7169 (2012).

[42] F. S. Soo and J. A. Theriot, Large-scale quantitative analysis of sources of variation in the ActinPolymerization-based movement of listeria monocytogenes, Biophys. J. **89**, 720 (2005).

[43] J. Slaghuis, M. Goetz, F. Engelbrecht, and W. Goebel, Inefficient replication of Listeria innocua in the cytosol of mammalian cells, J. Infect. Dis. **189**, 393 (2004).

[44] C. Kocks, J. B. Marchand, E. Gouin, H. D'Hauteville, P. J. Sansonetti, M. F. Carlier, and P. Cossart, The unrelated surface proteins ActA of Listeria monocytogenes and lcsA of Shigella flexneri are sufficient to confer actin-based motility on Listeria innocua and Escherichia coli respectively, Mol. Microbiol. **18**, 11 (1995).

[45] H. Choi, Z. Li, J. Zuponcic, E. Ximenes, J. Turek, M. Ladisch, and D. Nolte, Doppler Imaging Detects Bacterial Infection of Living Tissue, Communications Biology **4**, 178 (2020).